

# Evaluation of Underwater Sound Propagation of a Catamaran with Cavitating Propellers

Ulf Göttsche, Tobias Lampe, Martin Scharf, Moustafa Abdel-Maksoud

Institute for Fluid Dynamics and Ship Theory, Hamburg University of Technology, Hamburg, Germany

## ABSTRACT

The present article deals with the prediction of the underwater noise induced by ship propellers under consideration of sheet cavitation on the propeller blades. The calculation method is a hybrid approach combining a boundary element calculation method with the Ffowcs-Williams Hawkins equation. The capabilities of the method are demonstrated by simulating multiple operation states of the Newcastle University's catamaran research vessel, the "Princess Royal". The numeric results are compared to full-scale measurements.

## Keywords

Boundary element method, propeller noise, sheet cavitation, Ffowcs-Williams Hawkins, FWH

## 1 INTRODUCTION

The reduction of propeller noise has gained importance within the last years. Not only military vessels are affected by this issue, but also civil ship operators are faced with these problems due to already existing or coming international regulations. Thus, it is highly desirable to provide efficient and robust simulation tools capable of predicting propeller noise in an accurate manner. These tools need to be able to predict the acoustic far-field since this part of the acoustic domain dominates the environmental impact.

A direct simulation of the hydroacoustic field is a very complex and expensive task. In this work, an alternative and well established approach based on acoustic analogies is used (Ianniello et al. 2014a,b; Benschow and Liefvendahl 2016; Göttsche et al. 2017). The complex problem is split into two simpler problems: in a first step, the hydrodynamic properties of the considered body are calculated by conventional flow simulation methods in which the compressibility of the flow is neglected. Here, the in-house panel code *panMARE* (Berger 2018; Göttsche et al. 2017) is applied, which considers sheet cavitation on propellers. In a subsequent step, the hydroacoustic pressure in the far field is calculated by means of the Ffowcs-Williams Hawkins Equation (FWH-Equation) in Formulation 1A by Farassat and Brentner (1998) taking into account the hydrodynamic loads and displacement of the considered body as well as



**Figure 1:** Newcastle University's catamaran research vessel "Princess Royal" (Turkmen et al. 2017).

the compressibility of the fluid. In the method, a model to capture multiple sound reflections at the free water surface and at the ground is implemented.

The focus of the paper is to demonstrate the capabilities of the tool in an extensive numerical study. These are performed on the Newcastle University's catamaran research vessel, the "Princess Royal" (see Figure 1), for which the geometry and both model and full scale measurements are available (Atlar et al. 2013; Brooker and Humphrey 2016).

The calculation setup contains the submerged part of the hull and the fixed pitch propellers of each demi hull. The unsteady flow calculation of the hull and propeller is performed for multiple operation states specified in Brooker and Humphrey (2016) and Aktas et al. (2015). From these calculations, the hydroacoustic pressure is predicted for multiple measurements. Additionally, the contributions of different sound paths and sound sources are analyzed for selected observer points.

## 2 HYBRID SIMULATION METHOD

The underwater sound is yielded by a two step simulation method (Göttsche et al. 2017): In a first step, the flow field is calculated and the flow information of every time step is stored for the sound prediction. Afterwards in a post processing step, the underwater sound is calculated from the stored flow field values. This is done for every point of interest and can be repeated for arbitrary points.

### 2.1 Flow Calculation Method

For the flow calculation the in-house boundary element method *panMARE* is used (Göttsche et al. 2017; Berger 2018).

### 2.1.1 Governing Equations

The flow calculation is based on the potential theory. Following this, the flow is assumed to be irrotational, incompressible and inviscid. The governing equations are simplified to the Laplace Equation (1) for the velocity potential  $\Phi$  and the unsteady Bernoulli Equation (2) for the pressure  $p$  (Katz and Plotkin 2001):

$$\Delta\Phi = \nabla^2\Phi = 0 \quad (1)$$

and

$$p + \rho\vec{g}\vec{z} + \frac{1}{2}\rho(\nabla\Phi)^2 + \frac{\partial\Phi}{\partial t} = \text{const} \quad (2)$$

using fluid density  $\rho$ , gravitation  $\vec{g}$  and coordinate  $\vec{z}$ .

The velocity potential  $\Phi$  is a linear combination of the potential  $\Phi_{\text{move}}$  due to the movement of the body relative to the fixed frame coordinate system, the body influence as perturbation potential  $\Phi_{\text{ind}}$  and an arbitrary background flow  $\Phi_{\text{ext}}$ :

$$\Phi = \Phi_{\text{ind}} + \Phi_{\text{ext}} - \Phi_{\text{move}}. \quad (3)$$

One solution for Equation (1) is the Green identity:

$$\Phi_{\text{ind}} = \frac{1}{4\pi} \int_S \left[ \frac{1}{r} \nabla(\Phi - \Phi_I) - (\Phi - \Phi_I) \nabla \frac{1}{r} \right] \cdot \vec{n} dS. \quad (4)$$

In which  $\Phi_I$  is the velocity potential outside the fluid boundaries  $S$  and  $\Phi$  the potential in the fluid. The fluid boundaries consists of the outer boundaries  $S_B$  like bodies or free water surface and lifting body wake  $S_W$ . Additionally a source strength  $\sigma = \frac{\partial\Phi_I}{\partial n} - \frac{\partial\Phi}{\partial n}$  and dipole strength  $\mu = \Phi_I - \Phi$  is substituted:

$$\Phi_{\text{ind}} = \frac{1}{4\pi} \left[ \int_{S_B} \mu \frac{\partial}{\partial n} \frac{1}{r} - \sigma \frac{1}{r} dS + \int_{S_W} \mu \frac{\partial}{\partial n} \frac{1}{r} dS \right]. \quad (5)$$

The impermeability boundary condition on the outer boundaries and the Kutta boundary condition at lifting body trailing edges results in a unique solution. For additional details see Berger (2018).

### 2.1.2 Numerical Implementation

The boundaries of the fluid domain are discretised by quadrilateral panels with constant source and dipole strength on each. Combining Equation (5) with the boundary conditions mentioned above yields a system of linear equations. The solution of this equation system is the velocity distribution from which the Bernoulli Equation 2 delivers the pressure distribution.

### 2.1.3 Sheet Cavitation

The sheet cavitation is modeled by an approach based on the works of Fine (1992) and Vaz (2005) introducing additional boundary conditions. On the cavity surface  $S_{B_C} \subset S_B$  the dynamic boundary condition is applied which requires that the pressure equals the vapour pressure  $p_v$ . This leads to a Dirichlet-like formulation for the potential. Furthermore, the kinematic boundary condition on the surface of the cavity sheet is considered, which ensures that the surface is impermeable. From these conditions, the location of the boundary  $S_{B_C}$  is determined iteratively.

## 2.2 Sound Prediction Method

The sound prediction is performed by the Ffowcs-Williams Hawkins equation in Formulation 1A by Farassat (Brentner and Farassat 2003; Göttsche et al. 2017). This formulation uses the flow calculation results to determine the acoustic solution.

### 2.2.1 Theoretical Model

The Ffowcs-Williams Hawkins equation is a rearrangement of the Navier-Stokes equation and the continuity equation in the form of an inhomogeneous wave. Another interpretation is a generalized form of the Lighthill acoustic analogy.

$$p'_T(\vec{x}, t^*) = \frac{1}{4\pi} \int_S \left[ \frac{\rho_0(\dot{v}_n + v_{\dot{n}})}{r(1-M_r)^2} \right]_{\text{ret}} dS + \frac{1}{4\pi} \int_S \left[ \frac{\rho_0 v_n (r\dot{M}_r + cM_r - cM^2)}{r^2|1-M_r|^3} \right]_{\text{ret}} dS \quad (6)$$

$$p'_L(\vec{x}, t^*) = \frac{1}{4\pi} \frac{1}{c} \int_S \left[ \frac{\dot{l}_r}{r(1-M_r)^2} \right]_{\text{ret}} dS + \frac{1}{4\pi} \int_S \left[ \frac{l_r - l_M}{r^2(1-M_r)^2} \right]_{\text{ret}} dS + \frac{1}{4\pi} \frac{1}{c} \int_S \left[ \frac{l_r (r\dot{M}_r + cM_r - cM^2)}{r^2|1-M_r|^3} \right]_{\text{ret}} dS \quad (7)$$

$$p'(\vec{x}, t^*) = p'_T(\vec{x}, t^*) + p'_L(\vec{x}, t^*), \quad (8)$$

using the fluid density  $\rho_0$ , the body velocity  $\vec{v}$  relative to the undisturbed fluid, the distance vector  $\vec{r}$  as distance from the sound source point  $\vec{y}$  to the observer point  $\vec{x}$  with the norm  $r = \|\vec{r}\|$ , the Mach number  $\vec{M} = \frac{\vec{v}}{c}$ , the body surface  $S$ , the speed of sound  $c$  and the pressure force  $\vec{l} = p\vec{n}$  as pressure  $p$  on the body to the fluid in surface unit normal direction  $\vec{n}$ . A dot over a variable marks a time derivative of that variable. The subscripts  $n$ ,  $\dot{n}$ ,  $r$  and  $M$  imply a dot product of that vector variable and the unit normal vector  $\vec{n}$  of the surface into the fluid, the time derivative of the unit normal vector  $\vec{n}$ , the unit radiation vector  $\hat{r}$  or the surface velocity vector  $\vec{v}$  normalized by the sound speed  $c$  respectively. All values are taken from the source at a retarded time  $t_{\text{ret}}$  such that the information reaches the observer at time  $t^*$ . The term  $p_T$  (see Equation (6)) describes the influence of the body thickness, while  $p_L$  (see Equation (7)) describes the influence of the lifting forces. Terms with  $r^{-1}$  dependency are far-field terms, while terms with  $r^{-2}$  dependency are near-field terms.

The quadrupole term, which takes into account the contribution of the turbulence, is neglected, as the applied flow calculation method is not able to capture such information.

## 2.2.2 Implementation

The acoustic pressure is calculated at a point  $\vec{x}$  for a time  $t^*$ . As the flow calculation results are available on a discretised body surface  $S$  (see Section 2.1), the integral values from Equations (6) and (7) are rewritten as summation over the  $m$  body panels (Brentner and Farassat 2003).

$$p'_{T,i}(\vec{x}, t^*) = \left( \frac{\rho_0 (\dot{v}_n + v_{\dot{n}})}{r(1-M_r)^2} + \frac{\rho_0 v_n (r\dot{M}_r + c(M_r - M^2))}{r^2|1-M_r|^3} \right) \frac{S}{4\pi} \Bigg|_i \quad (9)$$

$$p'_{L,i}(\vec{x}, t^*) = \left( \frac{1}{c} \frac{\dot{l}_r}{r(1-M_r)^2} + \frac{l_r - l_M}{r^2(1-M_r)^2} + \frac{1}{c} \frac{l_r (r\dot{M}_r + c(M_r - M^2))}{r^2|1-M_r|^3} \right) \frac{S}{4\pi} \Bigg|_i \quad (10)$$

$$p'_i(\vec{x}, t^*) = p'_{T,i}(\vec{x}, t^*) + p'_{L,i}(\vec{x}, t^*) \quad (11)$$

$$p'(\vec{x}, t^*) = \sum_{i=1}^m p'_i(\vec{x}, t^*). \quad (12)$$

The time derivative of the pressure is approximated by a second order interpolation. All other values are taken from the flow calculation and assumed as constant on the panels.

The values on the body surface are taken at an emission time  $t_{\text{ret}} = t^* - \frac{\|\vec{x}(t^*) - \vec{y}(t)\|}{c}$ , respecting the sound speed  $s$ . Mostly the values must be interpolated from flow calculation time steps  $t_1 \leq t_{\text{ret}} \leq t_2$  to this retarded time  $t_{\text{ret}}$ . Instead of interpolating the flow values, the FWH pressure parts  $p'_i(\vec{x}(t^*), t_1 + \frac{r_1}{c})$  and  $p'_i(\vec{x}(t^*), t_2 + \frac{r_2}{c})$  are calculated at the two time steps and then a linear interpolation returns the final pressure part  $p'_i(\vec{x}(t^*), t^*)$ .

## 2.2.3 Reflection

In addition to the direct sound path calculated by the equations in Sections 2.2.1 and 2.2.2, a limited domain by free surface or sea bed contains reflection paths. This boundaries need not to be modeled in the flow calculation and are assumed to be planes.

In general, a reflected pressure can be calculated by mirroring the sources at the reflection plane and calculating the additional pressure contribution due to the new source. The signal loss of the reflection is calculated by the acoustic properties of the materials on both sides of the mirror plane, which leads to a reflection factor  $R$  correcting pressure  $p'_\Gamma$  of the path (Mei 2004):

$$R = \frac{m \cos^2 \Theta - n \sqrt{1 - \frac{\sin^2 \Theta}{n^2}}}{m \cos^2 \Theta + n \sqrt{1 - \frac{\sin^2 \Theta}{n^2}}} \quad (13)$$

$$p'_{\text{sum}}(\vec{x}, t^*) = p'(\vec{x}, t^*) + R p'_\Gamma(\vec{x}, t^*) \quad (14)$$

where  $m = \frac{\rho_1}{\rho}$  and  $n = \frac{c}{c_1}$ . The material properties are represented by the sound speed  $c$  and  $c_1$  and the density  $\rho$

**Table 1:** Propeller parameters (Aktas et al. 2015).

Characteristic	Value	
<i>Propeller</i>		
Propeller diameter	$D = 2R$ [m]	0.75
Pitch ratio at $r/R = 0.7$	$P_{0.7}/D$	1.06
Area ratio	$A_e/A_0$	1.06
Hub ratio	$d_h/D$	0.20
Number of blades	$z_P$	5

and  $\rho_1$  of the fluid and the material beyond the reflection plane. The incident angle is named  $\Theta$ .

At the free water surface Equation (13) returns a real value and is used there.

At the sea bed, which is more dense than the fluid, Equation (13) returns an imaginary value and cannot be used. Thus a material specific value between 0 (no reflection) and 1 (full reflection) is taken from measurements or literature.

## 2.2.4 Cavitation

If sheet cavitation on the body surface exists, the sheet surface is taken as emitting surface for the FWH pressure calculation. Therefore the motion of the body surface is superset with the change of the cavity thickness. The pressure on the surface can be used directly because the flow calculation already returns the vapour pressure.

## 2.2.5 Time to Frequency Domain Conversion

The method described so far operates in the time domain. Resulting values are converted to the frequency domain by a fast Fourier transform (FFT). To optimize the results, a sample of integer multiples of the most significant period, like propeller blade frequency, is taken from the time domain. Additionally, a Hanning window is used. The resulting pressure amplitudes from the FFT are converted to a power spectrum (single side autospectrum). This power spectrum is converted from  $[\text{Pa}^2]$  to  $[\text{dB}]$  with a reference value of  $1 \mu\text{Pa}$ , written as  $[\text{dB re. } \mu\text{Pa}^2]$ .

## 3 NUMERICAL STUDIES

Numerical studies are performed for various operation conditions of the Newcastle University's catamaran research vessel "Princess Royal" (Atlar et al. 2013). The vessel has a length of 18.9 m, a width a of 7.3 m and a draft of 1.83 m for the simulation (Aktas et al. 2015). Each demi hull has a five blade fix pitch propeller, each with a diameter of 0.75 m.

### 3.1 Open water characteristic

To verify the flow calculation, the open water characteristic of the starboard propeller is calculated. Each propeller blade is modeled by 20 panels in spanwise and 30 in chord direction for pressure as well as suction side (see Figure 2). The propeller wake is generated for 1.25 revolutions. The relevant simulation parameters are listed in Table 1.

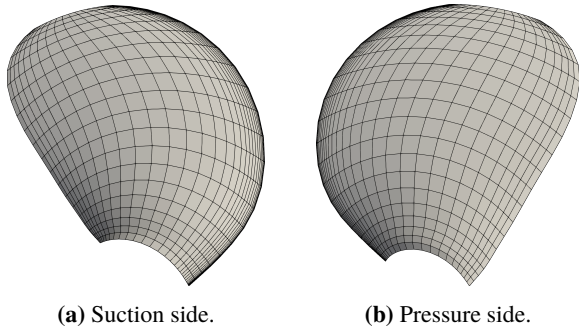


**Figure 2:** Propeller blade discretisation.

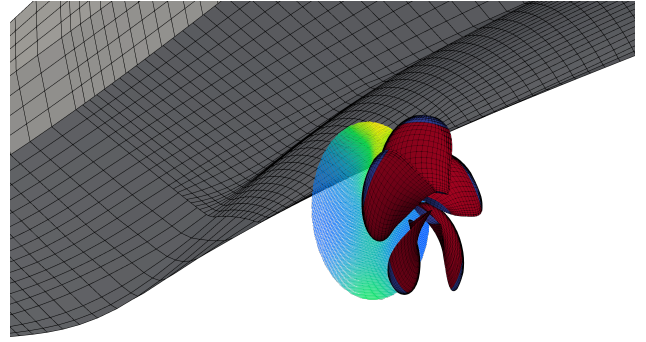


**Figure 4:** Discretised propeller and hull geometry.

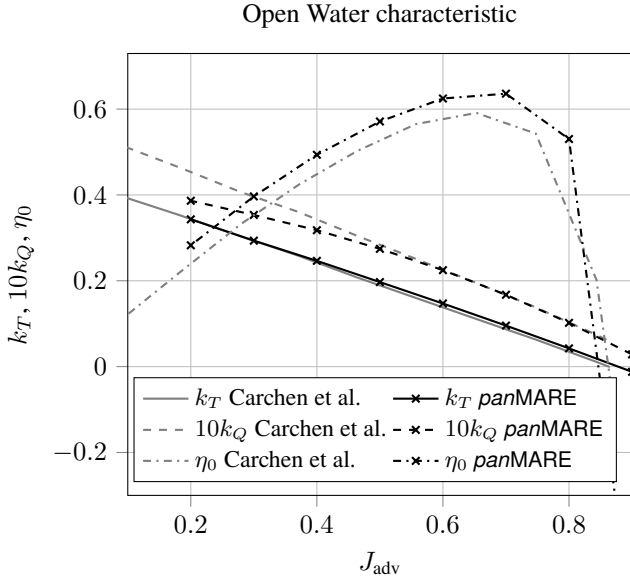


**Figure 3:** Open Water characteristic comparing published (Carchen et al. 2015) and *panMARE* values.

The calculated open water diagram is compared with published values by Carchen et al. (2015) in Figure 3. The agreement of the the thrust coefficient  $k_T$  in the publication and the calculated values in the range of  $J_{adv} \in [0.5, 0.8]$  is good. For small advance coefficients the calculated torque is below the reference values, which is a typical phenomena of boundary element calculations. The small disagreement in the efficiency  $\eta_0$  results from the existing differences in the thrust and torque coefficients.

### 3.2 Calculations setup

In order to evaluate the sound propagation, five different cases are calculated. In all cases the same discretized geometry is used, which is shown in Figure 4. Using the symmetry of the vessel, only the starbord demi hull is simulated in the flow calculation. The hull is modeled from the stern to 5.78 m in front direction and from keel to the undisturbed free water surface by 2624 panels (not all shown in Figure 4). The propeller discretisation is the same as in Section 3.1. On the blades, the panels, where cavitation is modeled, are colored in red and simple lifting panels at the blade tips and at the hub are marked in blue. The flow results from Section 3.1 show a complex flow behavior at

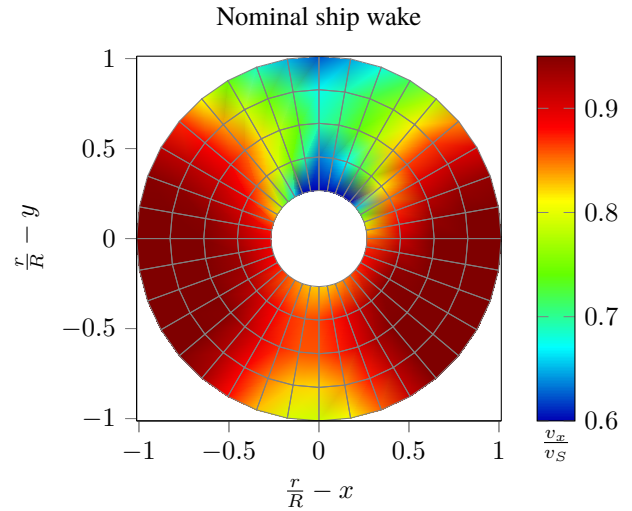


**Figure 5:** Nominal ship wake with axial flow velocity  $v_x$  normalised to ship's advanced speed  $v_S$  (Shi et al. 2018).

the blade tip which is not suitable for the cavitation model so far and therefore the outer four panel strips on the blades are also non-cavitating panels. The propeller wake is discretised for 2.5 revolutions (not shown in Figure 4), so that the influence of its starting vortex to the aft hull panels is negligible. To reduce the ship velocity to the correct inflow velocity for the propeller, the ship wake field is considered as known and modeled by 48456 points and located in a plane in front of the propeller, see Figure 4. Measured inflow velocities to the propeller are shown in Figure 5. The velocity distribution shown in Figure 4 corresponds to the wake distribution in Figure 5.

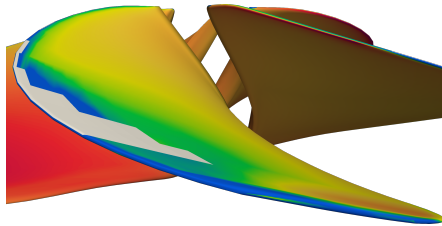
The calculated cases correspond to those measured in Brooker and Humphrey (2016) and Aktas et al. (2015). The simulation parameters are listed in Table 2. For the first two cases, no sheet cavitation occurred in the full scale measurements of Turkmen et al. (2017) and it is not modeled in the simulations.

### 3.3 Flow calculation

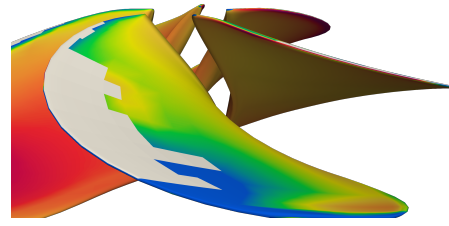
The flow calculations are performed for all five cases from Table 2. For every case six propeller revolutions are simulated to get periodic flow states in the last two revolutions for the sound prediction.

**Table 2:** Calculation parameters.

Characteristic			Values				
Case			#1	#2	#3	#4	#5
<i>Ship</i>							
Speed	$v_S$	[kn]	4.78	7.10	9.35	11.51	15.11
		[m s <sup>-1</sup> ]	2.46	3.63	4.81	5.92	7.77
<i>Propeller</i>							
Axis submersion	$d_S$	[m]	1.21	1.21	1.21	1.21	1.21
Rotation rate	$n$	[min <sup>-1</sup> ]	342.80	514.20	682.10	855.00	1141.50
		[s <sup>-1</sup> ]	5.71	8.57	11.68	14.25	19.03
Blade frequency	$f_B$	[Hz]	28.57	42.85	56.84	71.25	95.13
Angle per timestep		[°]	2.00	2.00	2.00	2.00	2.00
Thrust loading condition	$c_{Th}$		1.85	1.89	2.27	2.36	2.38
Cavitation number	$\sigma$		1.20	0.54	0.30	0.19	0.11
<i>Fluid</i>							
Fluid density	$\rho_0$	[kg m <sup>-3</sup> ]	1025.00	1025.00	1025.00	1025.00	1025.00
Vapour pressure	$p_V$	[Pa]			2500.00	2500.00	2500.00
Sound speed	$c_0$	[m s <sup>-1</sup> ]	1500.00	1500.00		1500.00	1500.00
<i>FWH</i>							
Air density	$\rho_1$	[kg m <sup>-3</sup> ]	1.29	1.29		1.29	1.29
Sound speed	$c_1$	[m s <sup>-1</sup> ]	343.20	343.20		343.20	343.20
Water depth	$d_G$	[m]	100.0	100.0		100.0	100.0
Sea bed reflection factor	$R_G$		0.50	0.50		0.50	0.50

(a) *panMARE*.

(b) Turkmen et al. (2017).

**Figure 6:** Cavitation pattern of Case #3.(a) *panMARE*.

(b) Turkmen et al. (2017).

**Figure 7:** Cavitation pattern of Case #4.

For the cases #1 and #2 no cavitation was observed and the flow field shows no conspicuities. Examples of the resulting cavitation patterns are presented for the cases #3 and #4 in Figure 6 as well as Figure 7 and compared to the full scale observations by Turkmen et al. (2017).

In case #3, Figure 6b shows the transition from leading edge vortex cavitation to sheet cavitation (Sampson et al. 2015). In comparison, the *panMARE* result shows an area of sheet cavitation. This results from the fact that *panMARE* cannot handle leading edge vortex cavitation so far and it produces

an unstable sheet cavitation pattern. Therefore the flow calculation is not comparable to the full scale observations and this case is not considered in the sound prediction in Section 3.4.

In case #4, the sheet cavitation pattern on the blade shown in Figure 7 are comparable with the computed cavity area. At the tip of the blades, where the cavitation is suppressed in *panMARE*, cloud cavitation occurs in the full scale observations (Sampson et al. 2015). As this is not accounted by

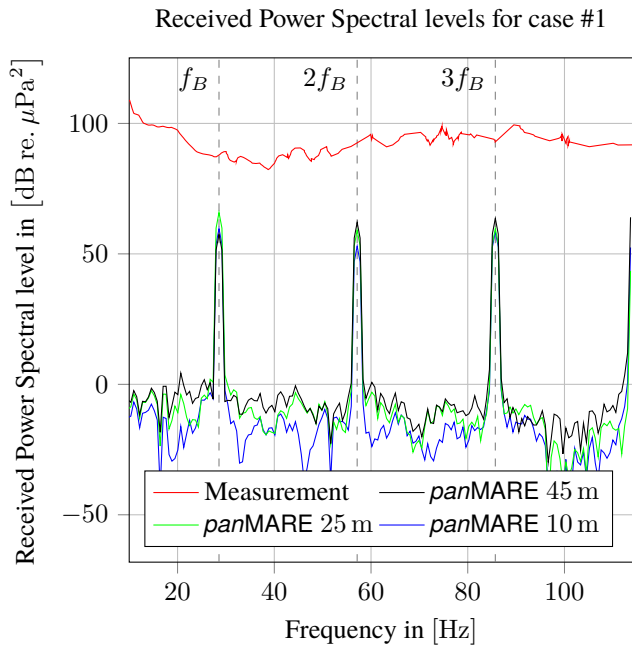


**Figure 8:** Received power spectral levels for case #1 comparing *panMARE* and Brooker and Humphrey (2016).

the simulation method and influences the flow negligibly, the flow can be assumed as similar.

### 3.4 Sound prediction

From the last two propeller revolutions of the flow calculation of the cases #1, #2, #4 and #5 a sound prediction is performed. The sound observation is done in a measurement plane at the propeller center normal to the vessels forward direction. The width of the plane is 110 m to both sides of the vessels center line and ranges from the sea bed to the free water surface. Therefore the observation points for comparison with Brooker and Humphrey (2016) are included in the plane. The observer points are placed 100 m aside the vessel center line in 10 m, 25 m and 45 m meter below the free surface. Three sound paths (direct, with free surface reflection and with ground reflection) are used to calculate the resulting sound pressure. The water depth is 100 m and the used sea bed reflection factor  $R_G$  is chosen as 0.5 (partial reflection).

As the flow calculation is performed only for the starboard demi hull, the hydroacoustic pressures are calculated on both sides of the vessel, mapped to the other side and summed to the resulting pressure distribution. From these symmetric hydroacoustic pressures in the time domain, the hydroacoustic sound values are calculated (see Section 2.2.5).

Following, examples of the acoustic results are presented.

For case #1, the received power spectral levels at the different observation points are shown in Figure 8 and compared to the measurements by Brooker and Humphrey (2016). Only the sum of sound paths are plotted. In Brooker and Humphrey (2016) the detailed pressure spectrums are given

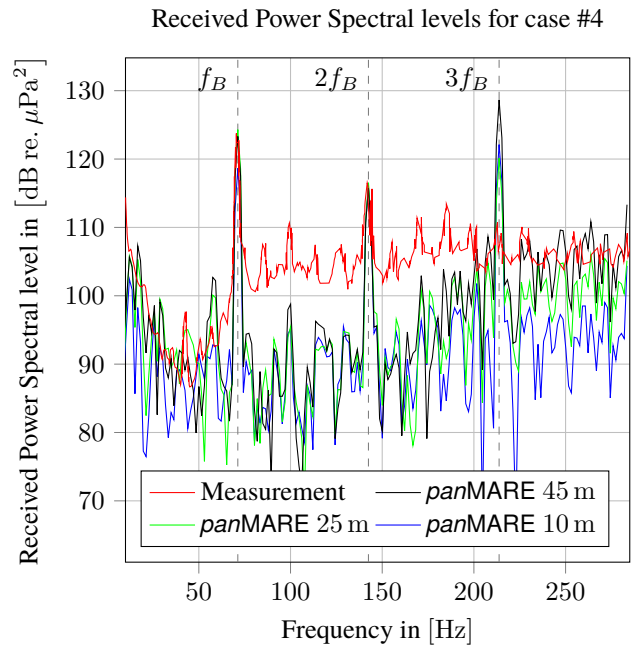


**Figure 9:** Received power spectral levels for case #4 comparing *panMARE* and Brooker and Humphrey (2016).

as the mean of the three hydrophones and in this paper the comparison is made against these mean values. As in this case cavitation does not take place, only the blade frequency  $f_B$  and its' multiple have values. The negative amplitudes between the blade frequency multiples are caused by the logarithmus of very small values. The amplitudes are clearly less than the measurement values, but in the measurement it is not clear, whether the measured results are dominated by the background sound spectrum as the contribution of the individual blade frequencies cannot be identified (Brooker and Humphrey 2016).

A similar picture occurs for case #2, which is not shown. There the amplitudes at the multiples of the blade frequencies are slightly larger than in case #1.

In Figure 9 the received power spectral levels of the sum paths of case #4 are shown. Here the calculated amplitudes match the measured values well. At the first and second blade frequency the difference for the observers at 25 m and 45 m depth is about 1 dB to the measurement values. The observer at 10 m depth has a difference to the measurement in the first blade frequency of 5 dB and 1 dB for the second blade frequency. At the third blade frequency, the values are clearly overestimated by more than 10 dB. Between the blade frequencies the calculated amplitudes are less than the measurement values. This should be expected, as not all noise sources are included in the simulation, such as turbulence, waves, structure, etc.

The different sound paths for the observer in 25 m depth are shown in Figure 10. For the first blade frequency the amplitudes of the sum of paths is less than 1 dB larger compared to the measurement value. The direct and free surface path amplitudes are about 7 dB larger and the sea bed path amplitudes are 2 dB less than the measured values.

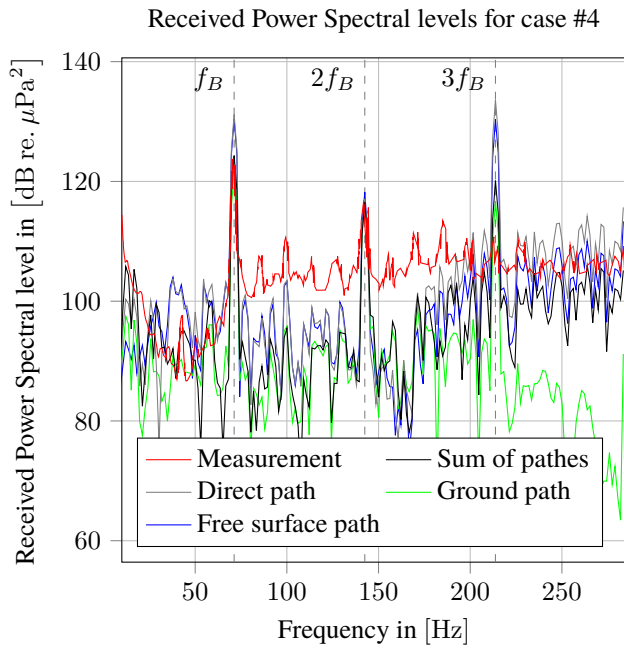


**Figure 10:** Received power spectral levels for case #4 comparing different paths in *panMARE* and Brooker and Humphrey (2016) for observer in depth 25 m.

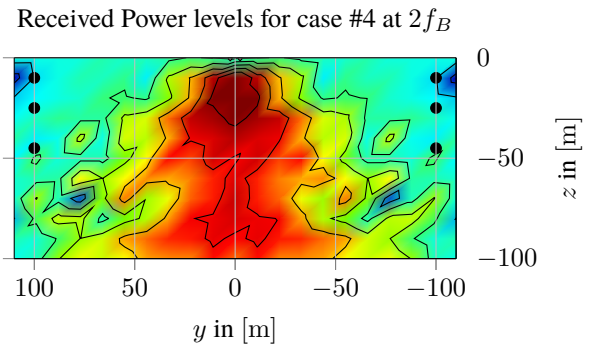
At the second blade frequency, all paths and the sum of paths has a difference less than 2 dB to the measurement. For the third blade frequency, all paths show amplitudes more than 10 dB larger than the measured amplitudes. This indicates a large interference for this frequency at this point.

Figure 11 shows the interference pattern of the sum of paths in the vertical measurement plane behind the vessel at the propellers center for the second and third blade frequency. On the port and starboard sides, the black circles mark the observer points. In Figure 11a the gradient of the interference pattern is small at the observer point at 25 m. This is also indicated in Figure 10 by the small difference between the different sound paths at the second blade frequency. On the other hand in Figure 11b shows a larger gradient at the observer point, which is indicated too by Figure 10's large differences in the sound paths at the third blade frequency.

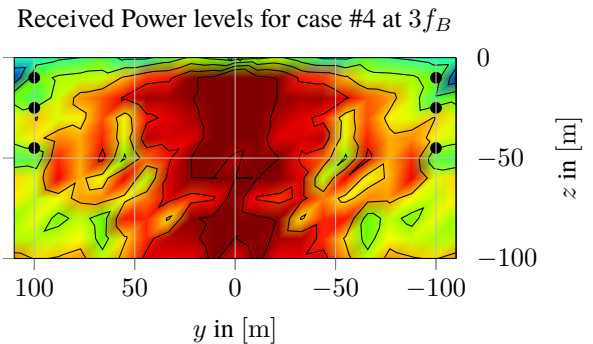
In Figure 12 the received power spectral levels of the sum paths of case #5 are shown. For this case there are no measurement by Brooker and Humphrey (2016) available. The amplitudes of the first and third blade frequency are up to 10 dB larger than in case #4. In this case, overall more interference is indicated by the larger difference between the sound paths. As result of this interference, at the second blade frequency no peak is present.

#### 4 CONCLUSION

In this paper the performance of a simulation method for the underwater noise emission prediction of non-cavitating and cavitating ship propellers was evaluated. In the prediction reflections at the sea bed and the free surface are considered. The results of different operation conditions of a vessel are compared with full-scale measurement data. In general a



**(a)** Second blade frequency  $2f_B = 142.50$  Hz.



**(b)** Third blade frequency  $3f_B = 213.75$  Hz.

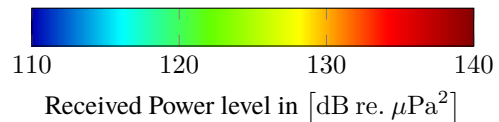


**Figure 11:** Received power level interference pattern for case #4 comparing first and third blade frequency.

good agreement of the calculated and the measured sound power spectral levels is achieved. Existing differences may arise due to difficulties in considering the environmental conditions and the different phase angle between the sound radiated by the twin propellers, which takes place during the full-scale situation and changes the interference pattern.

The accuracy of the computation was increased compared to the first presentation of the method (Göttsche et al. 2017) by modeling the exact ship hull. To improve this, the full-scale interference pattern should be analyzed and compared to the calculation results in detail. Additionally interaction of the propeller slip-stream and the rudder should be taken into account.

#### ACKNOWLEDGEMENTS

The authors are very grateful for the support of Prof. Mehmet Atlar and Dr. Batuhan Aktas, both from Newcastle University, for providing the measurement data of the Newcastle University's catamaran research vessel "Princess Royal" and the great help in explaining the details of the measurement campaigns.

The second author is funded by DFG (German Science Foundation – Deutsche Forschungsgesellschaft) under the

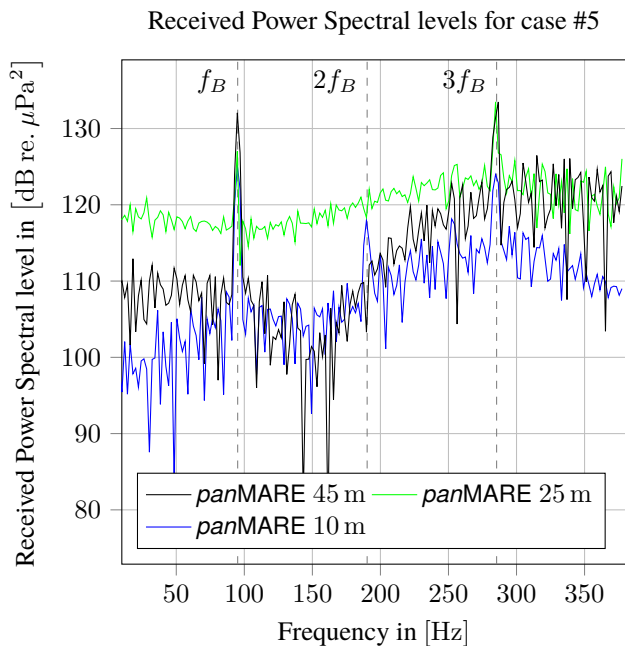


**Figure 12:** Received power spectral levels for case #5 of panMARE.

grant numbers AB 112/12-1 and the third author is funded by the BMWi-project (03SX461C) “ProNoVi”. The financial support is highly appreciated.

## REFERENCES

- Aktas, B., S. Turkmen, W. Shi, R. Sampson, E. Korkut, and M. Atlar (2015). “Underwater Radiated Noise Investigations of Cavitating Propellers Using Medium Size Cavitation Tunnel Tests and Full-Scale Trials”. In: *Fourth International Symposium on Marine Propulsors smp’15*. Ed. by S. A. Kinnas. Austin, Texas, USA, pp. 698–709.
- Atlar, M., B. Aktas, R. Sampson, K.-C. Seo, I. M. Viola, P. Fitzsimmons, and C. Fetherstonhaug (2013). “A multi-purpose marine science and technology research vessel for full-scale observations and measurements”. In: *3rd International Conference on Advanced Model Measurement Technologies for the Marine Industry – AMT’13*. Gdansk, Poland.
- Bensow, R. and M. Liefvendahl (2016). “An acoustic analogy and scale-resolving flow simulation methodology for the prediction of propeller radiated noise”. In: *31th Symposium on Naval Hydrodynamics*. Monterey, CA, USA.
- Berger, S. (2018). “Numerical Analysis of Propeller-Induced Higher-Order Pressure Fluctuations on the Ship Hull”. PhD thesis. Hamburg, Germany: Technical University of Hamburg. DOI: 10.15480/882.1605.
- Brentner, K. S. and F. Farassat (2003). “Modeling aerodynamically generated sound of helicopter rotors”. In: *Progress in Aerospace Sciences* 39.2–3, pp. 83–120. DOI: 10.1016/S0376-0421(02)00068-4.
- Brooker, A. and V. Humphrey (2016). “Measurement of radiated underwater noise from a small research vessel in shallow water”. In: *Ocean Engineering* 120, pp. 182–189. DOI: 10.1016/j.oceaneng.2015.09.048.
- Carchen, A., N. Sasaki, B. Aktas, S. Turkmen, and M. Atlar (2015). “Design and Review of the New NPT Propeller for the Princess Royal”. In: *4th International Conference on Advanced Model Measurement Technologies for the Marine Industry – AMT’15*. Istanbul, Turkey.
- Farassat, F. and K. S. Brentner (1998). “The Acoustic Analogy and the Prediction of the Noise of Rotating Blades”. In: *Theoretical and Computational Fluid Dynamics* 10.1, pp. 155–170. DOI: 10.1007/s001620050056.
- Fine, N. E. (1992). “Non-linear Analysis of Cavitating Propellers in Nonuniform Flow”. PhD thesis. Cambridge, USA: Massachusetts Institute of Technology.
- Göttsche, U., M. Scharf, S. Berger, and M. Abdel-Maksoud (2017). “A Hybrid Numerical Method for Investigating Underwater Sound Propagation of Cavitating Propellers”. In: *The Fifth International Symposium on Marine Propulsors – smp’17*. Ed. by A. Sánchez-Caja. Vol. 3. VTT Technical Research Centre of Finland Ltd. Espoo, Finland: VTT Technical Research Centre of Finland Ltd, pp. 520–527.
- Ianniello, S., R. Muscari, and A. Di Mascio (2014a). “Ship underwater noise assessment by the Acoustic Analogy. part II: hydroacoustic analysis of a ship scaled model”. In: *Journal of Marine Science and Technology* 19.1, pp. 52–74. DOI: 10.1007/s00773-013-0236-z.
- (2014b). “Ship underwater noise assessment by the acoustic analogy, part III: measurements versus numerical predictions on a full-scale ship”. In: *Journal of Marine Science and Technology* 19.2, pp. 125–142. DOI: 10.1007/s00773-013-0228-z.
- Katz, J. and A. Plotkin (2001). *Low-Speed Aerodynamics*. 2nd ed. Cambridge: Cambridge University Press, XVI, 613 S. DOI: 10.1017/CB09780511810329.
- Mei, C. C. (2004). *Wave propagation. Two dimensional waves*. URL: <http://web.mit.edu/1.138j/www/material/chap-3.pdf> (visited on 01/05/2017).
- Sampson, R., S. Turkmen, B. Aktas, W. Shi, P. Fitzsimmons, and M. Atlar (2015). “On the full scale and model scale cavitation comparisons of a Deep-V catamaran research vessel”. In: *Fourth International Symposium on Marine Propulsors smp’15*. Ed. by S. A. Kinnas. Austin, Texas, USA, pp. 250–260.
- Shi, W., B. Aktas, M. Atlar, D. Vasiljev, and K. Seo (2018). “Stereoscopic PIV aided wake simulation of a catamaran research vessel using a dummy-hull model in a medium size cavitation tunnel”. In: *Journal of Marine Science and Technology* 23.3, pp. 507–520.
- Turkmen, S., M. Atlar, and N. Sasaki (2017). “Full-Scale Measurements of Underwater Radiated Noise of a Catamaran Research Vessel”. In: *The Fifth International Symposium on Marine Propulsors – smp’17*. Ed. by A. Sánchez-Caja. Vol. 3. VTT Technical Research Centre of Finland Ltd. Espoo, Finland: VTT Technical Research Centre of Finland Ltd, pp. 503–509.
- Vaz, G. (2005). “Modelling of Sheet Cavitation on Hydrofoils and Marine Propellers using Boundary Element Methods”. PhD thesis. Lisbon, Portugal: IST, UTL.